International Journal of Mechanical Sciences 251 (2023) 108303

Contents lists available at ScienceDirect

International Journal of Mechanical Sciences

journal homepage: www.elsevier.com/locate/ijmecsci

A refined model for the effective tensile stiffness of Carbon NanoTube fibers

Laura Galuppi *, Vincenzo Andrea Muratore

Department of Engineering and Architecture, University of Parma, Parco Area delle Scienze 181/A, I-43124 Parma, Italy

ARTICLE INFO

Keywords:
Nanotube fiber
Micromechanics
Tensile response
Effective stiffness

ABSTRACT

The paper presents a solid-mechanics based method for the determination of the macroscopic tensile properties of fibers composed of monodispersed Carbon NanoTubes (CNTs), whose length is much lower than the fiber length, arranged in a cross-sectional square lattice. In the longitudinal direction, each CNT is offset, with respect to the neighboring ones, of a given quantity. The interaction between the CNTs caps is negligible, while the model takes into account the coupling occurring on their lateral surfaces, thanks to van der Waals forces and cross-links, modeled as distributed springs. One of the main improvements with respect to previous studies is that the CNTs are here modeled as deformable elastic bars, with given axial stiffness.

Under the assumption that, due to the periodicity of the CNTs arrangement, each CNT is subjected to the same loading state, it is demonstrated that the axial strain/stress fields are governed by a delayed-advanced differential equation, that is here solved by means of finite difference technique. This allows to evaluate the total axial force on the fiber, and, consequently, its *effective* tensile stiffness, strongly dependent on the length of the constituent CNTs, their offset and their axial compliance. Comparisons with literature data confirm the accuracy of the proposed approach.

1. Introduction

Carbon NanoTubes (CNTs) are cylindrical nanoscopic structures formed of one or more rolled-up graphite layers, with diameter of the order of 1 nm and typical length of 1÷5 μm. Their discovery in the first 1990s [1,2] inspired a flood of scientific activities worldwide, crossing several disciplines [3]. Indeed, due to their unique physical, thermal and electrical properties [4–6], such as high strength, low density, high conductivity and biological compatibility, they represent a very promising material for applications in nanoengineering [7,8], electronics [9,10], as well as in the biomedical field [11,12]. Notwithstanding their small size, discrete molecular structure and low wall thickness, CNTs were found to behave similarly to continuum structures with tensile and bending capacities, with exceptionally high Young's modulus (1 TPa [13,14]), and tensile strength of the order of 50 GPa [6]. In practical productions, CNTs may present different morphologies, as for example helical geometry [15,16], due to the introduction of defects.

Their exceptional properties make them the ideal material to be used in composites with improved mechanical properties. A typical example are nanocomposite polymers, formed of CNTs incorporated into host polymeric matrices [17–19], whose mechanical properties increase with the increasing of the amount of CNTs, of their dispersion and alignment in the polymeric matrix [20,21]. Other interesting CNT-based structures are bundles and fibers (Fig. 1) of weakly interacting tubes with compliant mobility associated with their relative sliding in the longitudinal direction. The interaction is due to the weak van der Waals forces [22], as well as to cross-linking [23,24].

CNT bundles (Fig. 1(a)), produced and studied mainly during the 1990s and the early 2000s, are composed of a limited number of CNTs (of the order of $10 \div 10^2$), and have diameter of about 10÷20 nm. On the other hand, fibers (Fig. 1(b)) with diameter of the order of 10÷100 μm, composed of a larger number of CNTs, are obtained by means of different techniques, that may be divided into "liquid" methods (wet spinning, [25,26]), where CNTs are dispersed into a liquid and solution-spun into fibers, and "solid" methods (dry spinning, [27,28]), where CNTs are directly spun into ropes or yarns. However, these processes yield fibers whose properties are not sufficiently close to optimal [29,30]. In more recent years, innovative high-throughput wet spinning procedures [31,32] have allowed to obtain macroscopic continuous fibers, composed of highly oriented and well-packed CNTs, with diameter up to 500 μm, and, in principle, no limit in terms of length. Remarkably, fibers obtained from helically coiled CNTs exhibit more tunable mechanical properties than those with straight ones and hold great potential for a wide range of applications [33,34].

Thanks to their very high strength-to-weight ratio, these kind of fibers, exhibiting mechanical properties competing with both high-strength fibers and metals, are ideally suited for high-value applications, for example in electronics [36] and biomedics [37,38]. Thanks

* Corresponding author.
E-mail addresses: laura.galuppi@unipr.it (L. Galuppi), vincenzoandrea.muratore@unipr.it (V.A. Muratore).

https://doi.org/10.1016/j.ijmecsci.2023.108303
Received 17 December 2022; Received in revised form 6 March 2023; Accepted 7 March 2023
Available online 24 March 2023

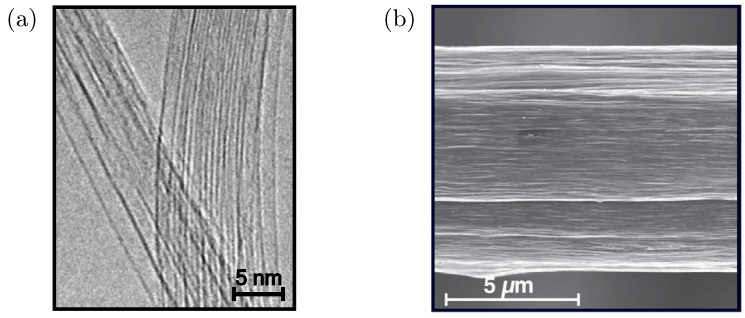

Fig. 1. (a) High-resolution TEM image of pristine single-walled CNT bundles [35] and (b) SEM image of the surface morphology of a CNT fiber [32].

to their flexibility, they can evolve into engineered materials, in the design of efficient light-weight aerospace structures, large-span bridges, and submarine structures [39,40]. The proper assessment of the *effective* mechanical properties of CNT fibers is of paramount importance for their possible use in macroscopic structural elements.

As discussed in [41], the macroscopic *tensile* stiffness of CNTs fibers is dictated by the compliance of the lateral bond between adjacent CNTs, dependent on their aspect ratio, arrangement and cross-link density and, in particular, by their overlapping length [41]. The latter is often neglected in analytical approaches (see, among the others, [42, 43], considering CNTs running along the entire fiber length), or taken into account as a random variable in molecular mechanic simulations [44,45]. In literature models based on solid mechanics [46,47], one of the main simplifying assumption consists into neglect the axial deformation of the CNTs composing the bundle/fiber, i.e., the constituent CNTs are modeled as axially rigid bars [41,48]. This usually leads to an overestimation of the macroscopic stiffness of the fiber.

This is why, in the refined model here proposed, the CNTs are modeled as deformable bars, with given axial stiffness. The considered model problem is that of a fiber composed of CNTs with length much lower than the fiber length, and connected along their lateral surfaces by means of distributed shear springs. CNTs are considered to be arranged in a square lattice in the fiber cross-section, of arbitrary shape, while in the axial direction they are offset of a given quantity with respect to the adjacent ones. These assumptions are similar to that adopted in [41], but in that study the CNTs were assumed to be axially rigid, and hence the fiber elongation was due to their axial displacement only. On the contrary, here they are modeled as deformable bars, whose axial compliance is accounted for, and consequently the fiber elongation results into both the axial displacement of the CNTs, and their elongation.

The axial response of the fiber is here studied by prescribing it a macroscopic elongation. In Section 2, the equation governing the resulting axial strain of the composing CNTs is obtained, by assuming that each CNT is subjected to the same actions, due to the periodicity of their arrangement. It is demonstrated that the problem is governed by a delayed-advanced differential equation, similar to those of nonlocal theories in continuum mechanics [49–51], whose solution is here found by means of finite difference technique. In Section 3, the obtained solution is used to evaluate the axial force acting on the fiber and, consequently, its axial stiffness, that turns out to be strongly dependent on the length of the constituent CNTs, their offset and their axial compliance. The obtained results show that the model allows for an accurate interpretation of experimental data.

2. Traction response of a fiber of NanoTubes

To investigate the tensile response of the CNT fiber, an approach similar to that adopted in [41] is used, i.e., a macroscopic elongation is prescribed to the whole fiber, and the correspondent axial force is evaluated *a posteriori*. In the aforementioned work, the constituent CNTs were assumed to be axially rigid, and hence the fiber elongation was given by the axial displacement of the CNTs. Here, the axial compliance of the CNTs is accounted for, and hence the macroscopic elongation results into two different-in-kind deformation mechanisms, occurring at the nanoscopic level, that will be detailed in the sequel: *(i)* the displacement in the axial direction of the CNTs composing the fiber and *(ii)* the (possibly non-uniform) stretch of the individual CNTs.

2.1. The model problem

The considered model problem is that of a fiber of length L, with cross section of arbitrary shape, with size of the order of $10\div100$ μm, as shown in Fig. 2. The fiber is composed of monodispersed CNTs, arranged in a regular square lattice in the cross-section (Fig. 2), with diameter d of the order of 1 nm and length $l \ll L$ of the order of $1\div10$ μm, so that the CNT aspect ratio is $l/d = 10^3 \div 10^4$. Here, we consider *compliant* single-walled[1] CNTs, with axial stiffness EA, where A is the cross sectional area and E the Young's modulus.

The offset between the caps of CNTs placed on the same longitudinal line allows their mobility in the longitudinal direction, and their interaction is negligible [52]. The shear coupling of adjacent CNTs on their lateral surface is due to the presence of van der Walls forces, and may be increased by cross-link [23,24]. Since the scale of the interaction is at the atomistic level, this may be modeled, from the mechanical point of view, by means of a soft thin interface layer [46,53], or with shear springs *à la* Winkler [41,54]. In the present model, we use the distributed shear springs shown in the magnified detail of Fig. 2(b), with linear response[2], and stiffness per unit length κ.

With reference to Fig. 2, introduce the reference system (x, y, z) with x on the direction of the fiber axis and y, z parallel to the lattice directions. In the cross-section, each y-"column" (z-"row", respectively) is constituted by a number of CNTs dependent on the z (y, respectively) coordinate. Following [41], the random axial misalignment of each CNT with respect to those belonging to adjacent lines is interpreted in an average way: when moving in the increasing y (respectively, z) direction, each CNT is offset (in the x direction) of ψl, with $\psi \in [0, 1]$, with respect to the "previous" one. The non-dimensional parameter ψ will be referred to as *offset parameter*. According to this spatial distribution, each CNT is connected to those composing the four adjacent "lines" in the y-column and z-row direction. Therefore, as emphasized in Fig. 2(c), each nanotube is connected with eight CNTs.

[1] The model can be easily extended to double-walled and multi-walled CNTs simply by correctly account for their cross area.

[2] More generally, the interaction between adjacent CNTs may be interpreted by means of non-linear springs [55].

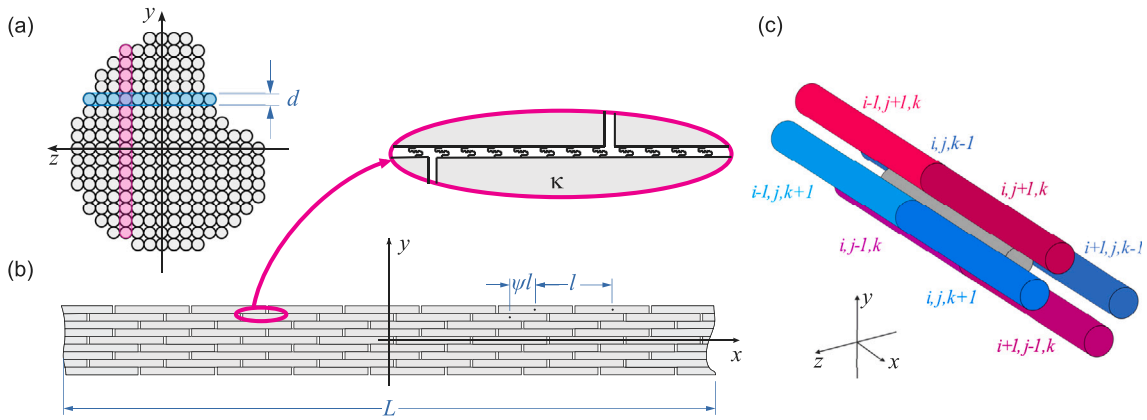

Fig. 2. Geometry of the considered CNT fiber, (a) cross and (b) longitudinal sections; (c) shear coupling of the (i, j, k) CNT.

2.2. Kinematics and loading state

By assuming that the CNTs are deformable bodies, when the CNT fiber undergoes a macroscopic deformation ϵ, this will produce two different mechanisms, namely: the axial displacement of the individual CNTs, moving apart from one another, and their elongation due to the forces transmitted by the springs, providing a traction load on the CNT itself. Due to the initial spacing between the CNT caps, and since their axial displacement increases the distance of their centroids, the CNT elongation does not affect the macroscopic stretch of the fiber. Hence, it can be assumed that the distance increase between the centroids of nanotubes belonging to the same line is homogeneous, and proportional to ϵ. As detailed in Appendix A.1, this allows to evaluate the CNTs position in the deformed configuration and, consequently, the relative displacement between points lying on adjacent CNTs.

A key point of the proposed model is that, due to the periodicity of the considered geometry, each CNT will be subjected to the same actions[3], transmitted by the shear springs. Hence, the axial displacement field, hereafter referred to as $u(\xi)$, where ξ is the local axial coordinate, $\xi \in [-l/2, l/2]$, will be the same on all the CNTs composing the fiber[4]. The shear forces (per unit length) transmitted by the springs, of stiffness κ, connecting the CNT to the adjacent ones are derived in Appendix A.1, and may be written as

$$\begin{aligned}
&t_{i,j+1,k}(\xi) = t_{i,j,k+1}(\xi) = \kappa\,[\psi l\epsilon + u(\xi - \psi l) - u(\xi)]\,,\\
&t_{i-1,j+1,k}(\xi) = t_{i-1,j,k+1}(\xi) = \kappa\,[-(1-\psi) l\epsilon + u(\xi + (1-\psi) l) - u(\xi)]\,,\\
&t_{i,j-1,k}(\xi) = t_{i,j,k-1}(\xi) = \kappa\,[-\psi l\epsilon + u(\xi + \psi l) - u(\xi)]\,,\\
&t_{i+1,j-1,k}(\xi) = t_{i+1,j,k-1}(\xi) = \kappa\,[(1-\psi) l\epsilon + u(\xi - (1-\psi) l) - u(\xi)]\,,
\end{aligned} \tag{2.1}$$

where pedex follow the notation of Fig. 2(c).

As schematically indicated in Fig. 3(a), the (i, j, k)th CNT can be divided in three regions,[5] where it is connected with different adjacent CNTs, namely: region A, with $\xi \in [-l/2, l(\psi - 1/2)]$; region B, with $\xi \in [l(\psi - 1/2), l(1/2 - \psi)]$; region C, with $\xi \in [l(1/2 - \psi), l/2]$.

The total force transmitted by the shear springs on the lateral surface of the CNT, hereafter denoted to as $t_{tot}(\xi)$, is the sum of the forces transmitted by the adjacent CNTs. Hence, on the diverse regions it takes different expressions, that are recorded in Appendix A.1.

2.3. Evaluation of axial force and displacement

The axial force $N(\xi)$ acting on the (i, j, k)th CNT is related to the axial displacement by

$$N(\xi) = EAu'(\xi)\,, \tag{2.2}$$

where $'$ denotes differentiation with respect to ξ, E is the CNT Young's modulus, of the order of 1 TPa [13,14,56], while A is the cross sectional area of the CNT. This may be evaluated as the area of the annulus (see, among the others, [52,57]) having mean diameter d and thickness s, corresponding to the thickness of the graphite layer, assumed equal to the interlayer spacing of graphite, i.e., 0.34 nm [58,59]. The axial force is related to the total shear forces transmitted by the distributed springs by the axial equilibrium of the CNTs, providing the differential relation

$$N'(\xi) = EAu''(\xi) = -t_{tot}(\xi), \tag{2.3}$$

taking different form in the different regions. In particular,

$$\begin{cases}
EAu''(\xi) = 2\kappa\,[-\epsilon l + u(\xi + (1-\psi)l) + u(\xi + \psi l) - 2u(\xi)] & \text{in region } A,\\
EAu''(\xi) = 2\kappa\,[u(\xi - \psi l) + u(\xi + \psi l) - 2u(\xi)] & \text{in region } B,\\
EAu''(\xi) = 2\kappa\,[\epsilon l + u(\xi - (1-\psi l)) + u(\xi - \psi l) - 2u(\xi)] & \text{in region } C.
\end{cases} \tag{2.4}$$

Continuity condition on both $u(\xi)$ and $N(\xi) = EAu'(\xi)$ should be required at the interfaces between adjacent regions. Furthermore, since the axial force is null at the ends of the CNTs, boundary conditions are

$$N(\xi)|_{\xi=-l/2} = EAu'(\xi)|_{\xi=-l/2} = 0, \quad N(\xi)|_{\xi=l/2} = EAu'(\xi)|_{\xi=l/2} = 0. \tag{2.5}$$

Eq. (2.4) is a *delayed-advanced* differential equation, where the derivative of the unknown function at a certain coordinate ξ depends on the function at other coordinates, with both a negative and a positive shift. Qualitatively, this stems from the fact that the value of $u(\xi)$ at a generic point ξ of the CNT depends on what happens at the "correspondent" points (i.e., points with the same axial *global* coordinate x) of adjacent CNTs, having a different *local* coordinate ξ. Due the symmetry of the problem (which causes the axial strain and stress field to be the same on each of the CNTs constituting the fiber), this value of $u(\xi)$ therefore depends on the value of the same function at different points on the same CNT.

This kind of equation is most frequently encountered when dealing with time evolution problems, where a time-dependent function

[3] This is not true for CNTs lying on the fiber surface, that are connected with less than 8 adjacent CNTs. However, since the cross-sectional area of the fiber is in general 4 (or even 5) orders of magnitude higher than that of CNTs, the contribution of the external CNTs may be considered to be negligible.

[4] Notice that other models proposed by the literature, based on similar approaches [46,47], consider the interaction between only two adjacent CNTs, so neglecting both the complex mutual interaction between the CNT lattice, and the periodicity of the considered problem. Roughly speaking, these models do not consider that the axial displacement/strain/stress fields must be the same on *all* the CNTs composing the fiber.

[5] Obviously, for $\psi = 0.5$ (i.e., for CNTs offset by exactly half their own length) the end of region A (at $\xi = 0$) coincides with the beginning of region C, while the length of region B is nil.

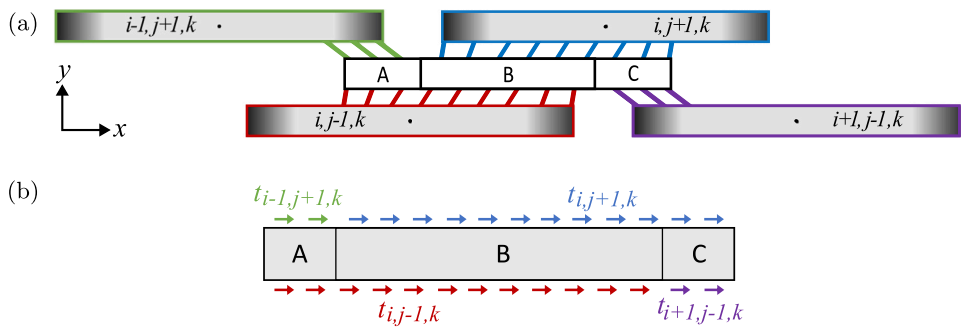

Fig. 3. (a) Different regions defined on the (i, j, k)th CNT, and (b) forces transmitted by CNTs acting on the (i, j, k)th CNT, on the (x, y) plane.

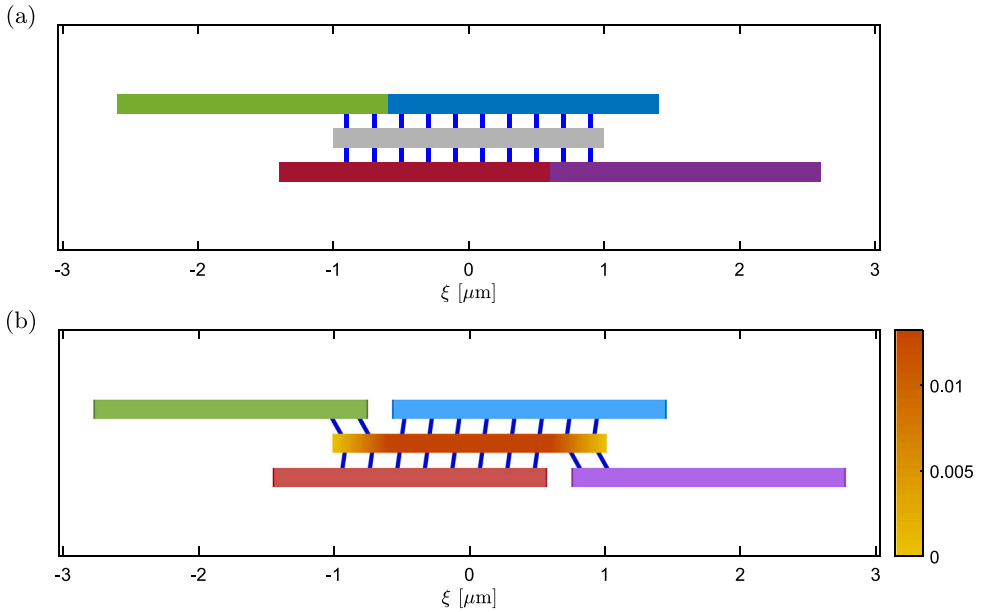

Fig. 4. Case $l = 2$ μm, $\psi = 0.2$. (a) Undeformed and (b) deformed configuration of the (i, j, k)th CNT and of its neighboring CNTs, on the (x, y) plane, with plot of the axial strain $\epsilon(\xi)$ on the (i, j, k)th CNT.

depends on both the current state, and the previous and subsequent states. Applications can be found in electronic, physics, biology, and economy fields [60,61], as well as in non-local elasticity [49,62] and in peridynamic theory [50,63,64]. The exact solution of this class of equations is a very difficult task [65], and it is usually found by means of numerical techniques (see, among the others, [60,66,67]).

2.4. Results and comparisons

The delayed-advanced differential eq. (2.4) is numerically solved by means of the finite difference technique, allowing to evaluate both the axial displacement $u(\xi)$ and the axial force $N(\xi)$. The details of the implementation may be found in Appendix A.3. This allows to evaluate *a posteriori* the relative slips between adjacent CNTs and the shear forces transmitted by the distributed springs. In Appendix A.2, the results are analytically compared with the closed-form solution obtained in [41] for the case of fiber composed of rigid CNTs. In the sequel, the influence on the displacement field of the CNT length and offset is studied.

2.4.1. Results in terms of axial displacement and axial force

Consider, as a reference example, a fiber composed single-walled CNTs with diameter $d = 1$ nm, and Young modulus $E = 10^6$ MPa. The axial stiffness of the individual CNT is, hence, $EA = 1.068\ 10^{-6}$ N. According to [41], the stiffness of the shear springs[6] connecting the adjacent CNTs is assumed to be $\kappa = 0.1$ MPa. For these parameters, Fig. 4(a) shows the arrangement of the reference (i, j, k)th CNT and of its neighboring ones, for CNT length $l = 2$ μm and offset parameter $\psi = 0.2$, in the undeformed (reference) configuration, while Fig. 4(b) shows CNTs arrangement and deformation due to a prescribed macroscopic fiber deformation $\epsilon = 10\%$.

It may be noticed from Fig. 4(b) that the CNTs not only move away from each other, but also elongate. To clearly appreciate the extent of this deformation in the figure, the representation of the CNTs with initial length (shown with light colors) is superimposed on that of the actually deformed CNTs (shown with darker colors). The axial strain $\epsilon(\xi) = u'(\xi)$ in the (i, j, k)th CNT is plotted, with colorbar, on the same Figure. Notice that the CNT is not uniformly strained, i.e., $\epsilon(\xi)$ is higher in the central part of the CNT, while being null at its ends.

[6] Unfortunately, the scientific literature does not provide univoque values for the shear stiffness of van der Waals bonding, that is highly dependent on several chemical and geometrical parameters, as, for example, the CNT chirality [68,69] and the spacing between adjacent CNTs [46]. Furthermore, the shear stiffness of the bonding can be consistently increased by means of cross-links (see, among the others, [45,47,70]). Hence, in order to compare the proposed analytical model with that of [41], we consider the same value κ=0.1 MPa recorded in that paper.

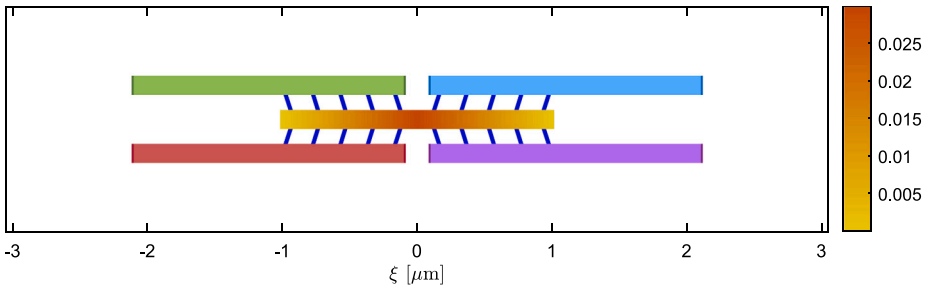

Fig. 5. Case $l = 2$ μm, $\psi = 0.5$. Deformed configuration of the (i, j, k)th CNT and of its neighboring CNTs, on the (x, y) plane, with plot of the axial strain $\epsilon(\xi)$ on the (i, j, k)th CNT.

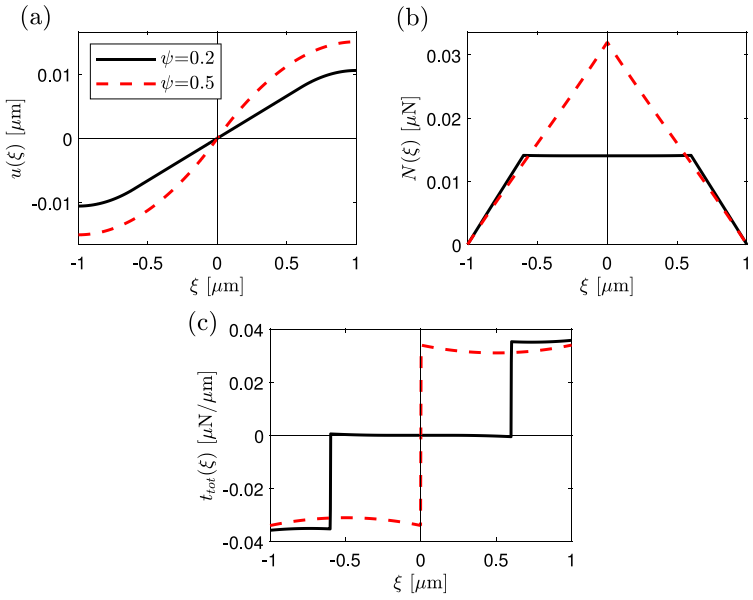

Fig. 6. Case $l = 2$ μm. (a) Axial displacement field $u(\xi)$, (b) axial force $N(\xi)$, (c) total shear force $t_{tot}(\xi)$.

To investigate the influence on the CNT axial strain of the offset parameter ψ, now the case $\psi = 0.5$ is considered. Fig. 5 shows the arrangement of CNTs, with $l = 2$ μm and $\psi = 0.5$, before and after the deformation.

For the cases $\psi = 0.2$ and $\psi = 0.5$, Fig. 6(a) shows the axial displacement $u(\xi)$ of the CNT (to avoid rigid body displacement, here $u(\xi)|_{\xi=0} = 0$ has been set). As expected, due to the symmetry of the considered problem, the displacement field is anti-symmetric. Graph in Fig. 6(b) records the axial force $N(\xi) = EAu'(\xi)$, varying along the axial coordinate of the CNT. Fig. 6(c) show the trend of the total shear force $t_{tot}(\xi)$ (A.7) transmitted by the adjacent CNTs.

It may be observed that, for $\psi = 0.2$, $t_{tot}(\xi)$ is approximately constant in region A and C, while being almost nil in the central region B. Noticeably, this solution is qualitatively very similar to that obtained by adopting the assumption of rigid CNTs (see Appendix A.2). On the other hand, for $\psi = 0.5$, the variation of the total force $t_{tot}(\xi)$ along the ξ coordinate is more relevant than that recorded for $\psi = 0.2$. This indicates that the deformability of the individual CNTs plays a more important role for high values of axial offset. It may also be noticed that, for $\psi = 0.5$, $N(\xi)$ takes high values in the central region of the CNT, hence resulting in a high value of strain in proximity of $\xi = 0$.

To investigate the influence of the CNT length on its axial displacement field, now a fiber composed of CNTs 5 μm long is considered, while leaving unchanged the other relevant parameters. Figs. 7(a) and 7(b) show the arrangement of CNTs, for the cases $\psi = 0.2$ and $\psi = 0.5$, respectively. For the same cases, Fig. 8 shows the axial distribution of the axial displacement and of the axial force in each CNT, as well as the total shear forces.

It may be noticed from Fig. 7 that, in this case, the elongation of the individual CNTs is consistently higher than that observed in Figs. 5 and 4(b). Furthermore, by comparing Fig. 8 with its counterpart for CNTs 2 μm long (Fig. 6), it may be observed that, for longer CNTs, the (non-linear) variation of the total force along the ξ axis is much more relevant. Notice, in particular, that for the case $\psi = 0.5$ the axial strain tends to localize in the neighboring of the interface between the two regions ($\xi = 0$). It may be verified that this phenomenon is even more relevant for higher values of l (graphs are not recorded here for the sake of brevity). This is because, for very high CNT length (or, equivalently, for very low axial stiffness of the CNTs, or for high stiffness of the distributed springs), the forces exerted by the springs tend to concentrate at the interface between region A and C. Correspondingly, the axial force $N(\xi)$ tends to become constant along ξ, with a Dirac delta arising at $\xi = 0$. Obviously, this kind of response cannot be captured by the simpler model of [41].

The particular case of null axial offset ($\psi = 0$) corresponds to a configuration with vertically stacked CNTs. As already observed in [41], in this case the fiber is underconstrained and cannot bear axial loads, because the stacks can move independently one another. Therefore, both the displacement and strain fields are null, as well as the forces transmitted by the (not-deformed) shear distributed springs.

For all the considered cases, the numerical model allows to evaluate the resultant of the shear forces acting, on the (x, y) plane, on the lower

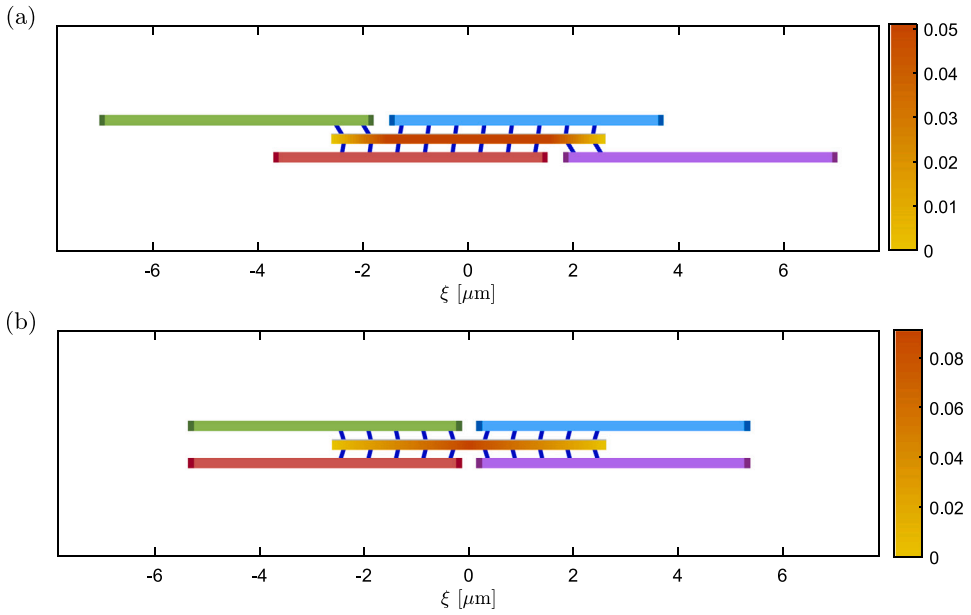

Fig. 7. Case $l = 5$ μm. Deformed configuration of the (i, j, k)th CNT and of its neighboring CNTs, on the (x, y) plane, with plot of the axial strain $\varepsilon(\xi)$ on the (i, j, k)th CNT. Cases (a) $\psi = 0.2$ and (b) $\psi = 0.5$.

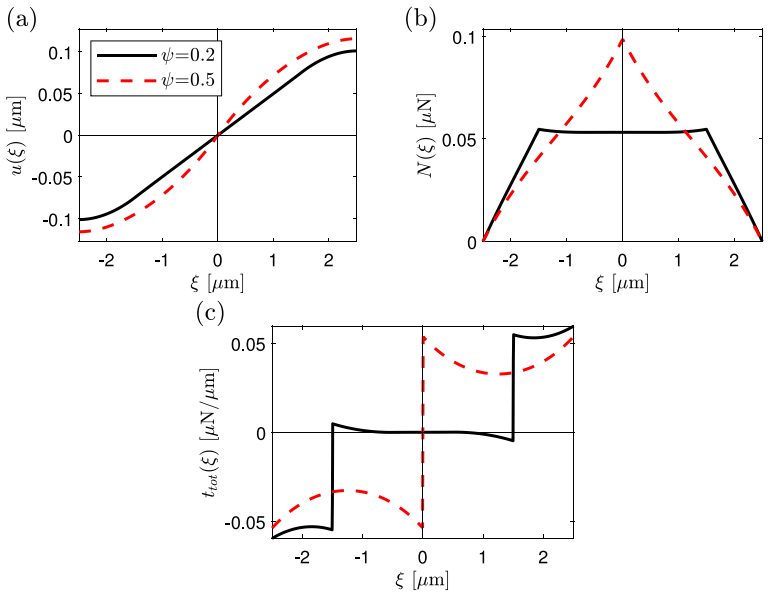

Fig. 8. Case $l = 5$ μm. (a) Axial displacement field $u(\xi)$, (b) axial force $N(\xi)$, (c) total shear force $t_{tot}(\xi)$.

part of the CNT (i.e., in the direction of decreasing y), and on its upper (direction of increasing y) part, i.e.,

$$T_{y^-} = \int_{-l/2}^{l(1/2-\psi)} t_{i,j-1,k}(\xi)\, d\xi + \int_{l(1/2-\psi)}^{l/2} t_{i+1,j-1,k}(\xi)\, d\xi,$$
$$T_{y^+} = \int_{-l/2}^{l(\psi-1/2)} t_{i-1,j+1,k}(\xi)\, d\xi + \int_{l(\psi-1/2)}^{l/2} t_{i,j+1,k}(\xi)\, d\xi. \tag{2.6}$$

Obviously, due to the symmetry of the problem, on the (x, z) plane the resultants will be $T_{z^-} = T_{y^-}$ and $T_{z^+} = T_{y^+}$. To satisfy the rotational equilibrium about the y and z axes, all the resultants must be nil (so to not give rise to couples), i.e.,

$$T_{z^-} = T_{y^-} = T_{z^+} = T_{y^+} = 0. \tag{2.7}$$

This obviously satisfies also the equilibrium in the axial direction. Condition (2.7) has been numerically verified, confirming the accuracy of the obtained solution. Remarkably, this will be useful for the evaluation of the effective tensile stiffness of the CNT fiber, as it will be discussed in Section 3.2.

2.4.2. CNT relative elongation and strain energy

The results presented in the previous subsection suggest that the axial strain of the CNTs is higher for long CNTs, and for high values of axial offset. To deeply investigate this phenomenon, consider the strain energy of a single CNT, correspondent to the energy "spent" to deform it, defined as

$$\mathcal{E}_{CNT} = \frac{1}{2}\int_{-l/2}^{l/2} N(\xi)u'(\xi)\, d\xi = \frac{EA}{2}\int_{-l/2}^{l/2} \left[u'(\xi)\right]^2\, d\xi. \tag{2.8}$$

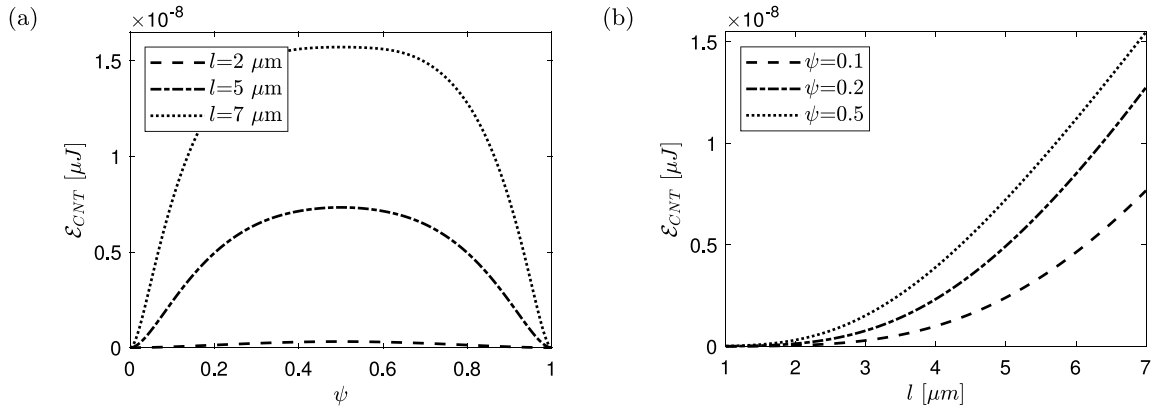

Fig. 9. Strain energy of the individual CNT (a) as a function of ψ, for different values of l and (b) as a function of l, for different values of ψ.

In Fig. 9(a), $\mathcal{E}_{CNT}$ is plotted as a function of the offset parameter ψ, for different values of the CNT's length ($l = 2,\ 5,\ 7$ μm). Obviously, the graph is symmetric, because the case $\psi \in [0.5, 1]$ may be treated by considering, instead of ψ, the value $1 - \psi$. Obviously, for the stacked configuration ($\psi = 0,\ 1$), the strain energy is null. Fig. 9(b) is the counterpart of Fig. 9(a), showing $\mathcal{E}_{CNT}$ as a function of l, for different values of ψ.

It is evident that the strain energy is strongly dependent upon the CNT length and offset, being higher for long and highly coupled CNTs (i.e., for high values of ψ). Fig. 9(b) highlights how the dependence of $\mathcal{E}_{CNT}$ on the CNT length is superlinear.

Let us consider now the relative elongation of the individual CNTs, $\Delta l/l$, that is strongly dependent on their axial stiffness, and on the stiffness κ of the distributed springs. By defining a coefficient $\beta := EA/\kappa$, the following non-dimensional quantity may be defined

$$\phi(\beta, l, \psi) := \frac{\Delta l}{\epsilon l} = \frac{1}{\epsilon l}\int_{-l/2}^{l/2} u'(\xi)\, d\xi, \tag{2.9}$$

correspondent to the ratio between the relative elongation of the individual CNTs and the prescribed macroscopic deformation ϵ, correspondent to the displacement of their centroids along the fiber axis (independent on l and ψ, as discussed in Section 2.2). It may be verified that, due to the linearity of the considered problem, $\phi(\beta, l, \psi)$ is independent of ϵ. It is expected to vary between 0 (when the CNTs are rigid and hence $\Delta l = 0$, and when they are stackered), and 1 (when the CNTs are very deformable with respect to the shear springs, and hence all the prescribed deformation results in an elongation of the individual CNTs). Indeed, in the latter case, the axial displacement may be evaluated by requiring that the relative displacement of adjacent CNTs is null, and turns out to be in the form $u(\xi) = \epsilon\xi$, hence providing $\Delta l = \epsilon l$ and, consequently, $\phi(\beta, l, \psi) \to 1$. Hence, $\phi(\beta, l, \psi)$ may be regarded as a "measure" of the relevance of the two deformation mechanisms described at the beginning of Section 2. This will be discussed more in detail in Section 3.3.1.

Fig. 10(a) shows $\phi(\beta, l, \psi)$ plotted as a function of the offset parameter ψ, for the same values of l considered in Fig. 9(a). Fig. 10(b) is the counterpart of Fig. 10(a), showing $\phi(\beta, l, \psi)$ as a function of l, for different values of ψ.

As expected from previous results, the relative elongation of the CNTs increases as their length and offset increase. With reference to the two deformation mechanisms described at the beginning of Section 2, this means that the stretch of the individual CNTs becomes more relevant, with respect to the displacement of their centroids along the fiber axis, for long and highly offset CNTs.

Notice that, for low values of l, the dependence on the offset parameter ψ is approximately parabolic, while for higher values of l it takes a more complicated dependence on ψ. In particular, in the latter case, $\phi(\beta, l, \psi)$ is almost constant for a wide range of values of ψ, taking lower values for $\psi \simeq 0.5$. This is because, as discussed in Section 2.4.1, in this case the strain tends to concentrate only in the central region of the CNTs. It may be verified that this phenomenon is even more relevant for higher values of l.

3. Effective tensile stiffness

The displacement field determined in Section 2 allows to evaluate the macroscopic stiffness of the whole CNT fiber. This may be done by considering the fiber as an equivalent homogeneous beam, subjected to a macroscopic deformation ϵ, whose *effective Young's modulus* E_f can be defined as

$$E_f = \frac{N_f}{A_f \epsilon}, \tag{3.1}$$

where A_f is the cross-sectional area of the fiber, of arbitrary shape, while N_f is the total axial force acting on the fiber itself, that may be evaluated as the sum of the axial forces acting on the individual CNTs. To calculate N_f, it is important to proper account for the CNTs distribution in the fiber cross section.

In the sequel, first the simple case where the fiber may be considered as formed of "bunches" composed of a integer number of CNTs is considered, for the sake of explanation, and hence the more general case is treated.

3.1. Simple case

Consider first the simple case where $\psi = 1/n_b$, being n_b a natural number. Recall that, as discussed in Section 2, the CNTs are assumed to be arranged in the fiber cross-section according to a square matrix, allowing their distribution to be the same on the (x, y) and (x, z) planes. Since the distribution of CNTs on each row/column repeats periodically every n_b CNTs, it is possible to identify "bunches" composed of n_b CNTs on each row/column composing the fiber cross section. Due to the periodicity, the bunches are equal one to each other, and repeat on each row/column (i.e., on both the (x, y) and the (x, z) planes). This kind of subdivision is illustrated in Fig. 11, referring to a fiber[7] composed of CNTs offset in the axial direction of 1/5 of their length (i.e., $\psi = 0.2$), where "bunches" of 5 CNTs may be identified on both the y and z directions. In the sequel, for simplicity we will refer to bunches lying on the (x, y) plane.

Due to the periodicity of the considered structure, each bunch carries the same axial load, hereafter denoted to as N_b. This may be evaluated by sectioning the bunch as shown in Fig. 12, at a generic distance αl, with $\alpha < \psi$, from the left end of the first CNT.

[7] For the sake of example, without loss of generality, in Fig. 11 a CNT fiber with circular cross section is shown. However, the proposed approach can be used for any shape of the cross section.

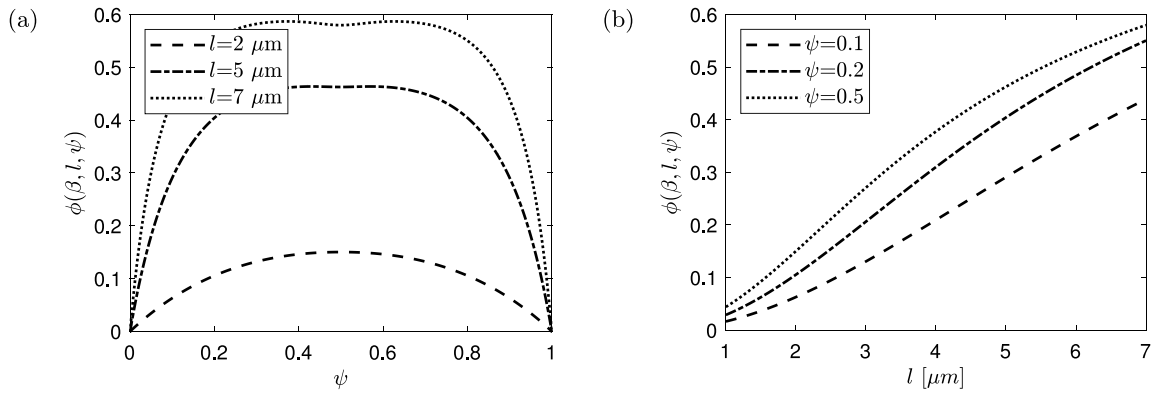

Fig. 10. Non-dimensional function $\phi(\beta, l, \psi)$ (a) as a function of ψ, for different values of l and (b) as a function of l, for different values of ψ.

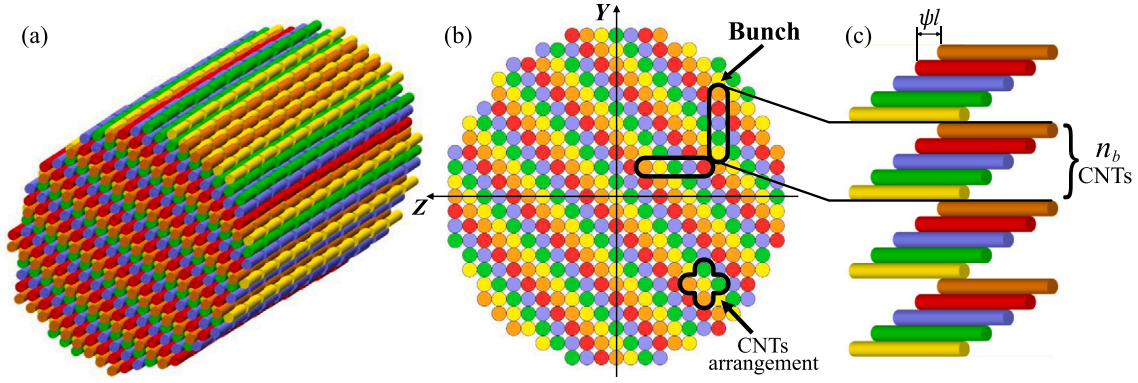

Fig. 11. Section of the CNT fiber: (a) 3D and (b) 2D view, and (c) detail of the CNT bunch. Different colors indicate different axial position of the CNTs.

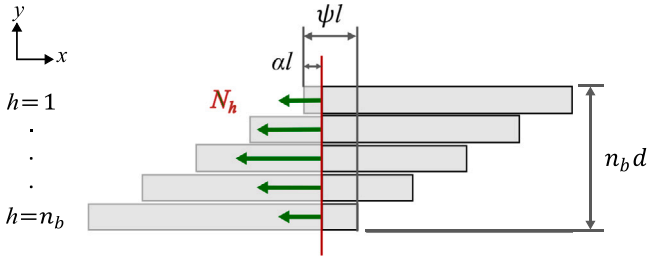

Fig. 12. Sectioning the bunch.

Notice that this correspond to section each CNT composing the bunch at a different coordinate ξ. Consequently, by numbering the CNTs composing the bunch with the pedex $h = 1 \dots n_b$ as in Fig. 12, the axial force acting on the hth CNT may be evaluated as

$$N_h = N(\xi)|_{\xi=-l/2+\alpha l+(h-1)\psi l}. \tag{3.2}$$

Consequently, the normal force on the whole bunch is given by

$$N_b = \sum_{h=1}^{n_b} N_h = \sum_{h=1}^{n_b} N\left(-l/2 + \alpha l + (h-1)\psi l\right). \tag{3.3}$$

It has been numerically verified that N_b is independent of the parameter α. This is a noteworthy result, confirming that, even if the axial force on the individual CNTs is highly variable along their axis (see Figs. 6 and 8), their resultant on the bunch is uniform. Once N_b is known, the total force acting on the fiber may be evaluated by summing the contributions of all the bunches. Observing that the "area of competence" of each bunch is

$$A_b = n_b d^2 = \frac{d^2}{\psi}, \tag{3.4}$$

and consequently the total force N_f may be evaluated as

$$N_f = \frac{A_f}{A_b} N_b = \frac{\psi A_f}{d^2} N_b. \tag{3.5}$$

3.2. General case

The approach proposed in Section 3.1 can be used only if the bunch is composed of an integer number $n_b = 1/\psi$ of CNTs, while the case where ψ is a generic real number may be treated in a more general way. To illustrate it, consider the CNT bunch of Fig. 11, sectioned with $\alpha = 0$, as shown in Fig. 13(a). Consider also the cut with "saw-toothed profile" indicated with dashed line in the same Figure, formed of n_b inclined cuts with slope $-\psi l/d$.

Let us consider the equilibrium, in the axial direction, of the portion comprised between these two "cuts", as shown in Fig. 13(b). As schematized in the same Figure, on the l.h.s. each CNT, of diameter d, is subjected to the axial forces N_h (3.2), while on the inclined cut the force $\frac{N(\xi)}{d} d\eta$ arise on the infinitesimal $-d\eta$. Furthermore, the portion of bunch is also subjected to the shear forces[8] acting on the lower part of the CNTs, correspondent to $t_{i,j-1,k}(\xi)$ (in regions A and B) and $t_{i+1,j-1,k}(\xi)$ (in region C, see also Fig. 3(a)).

The equilibrium of this portion of the bunch may be evaluated in a very simple way. Indeed, by "translating" each CNT of ψl in the axial direction, as shown in Fig. 14, it is evident that the inclined cut covers all the CNT length.

[8] Recall that, due to the periodicity of the problem, each CNT is subjected to the same action configuration.

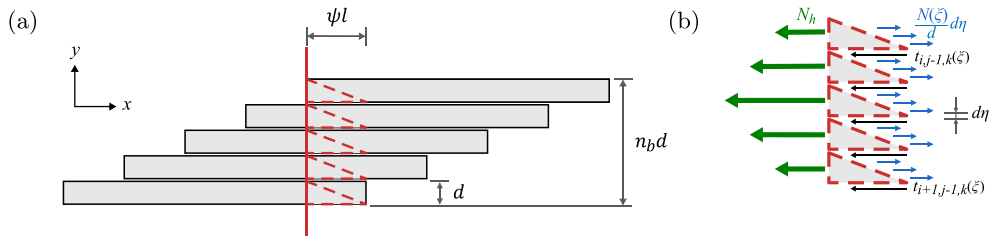

Fig. 13. (a) Cut with "saw-toothed profile"; (b) Equilibrium of the portion between the cuts.

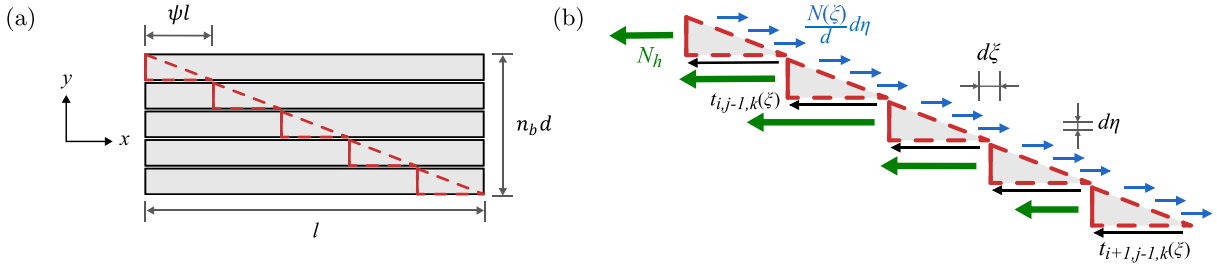

Fig. 14. (a) "Translating" each CNT of ψl in the axial direction; (b) The inclined cut covers all the CNT length.

Recalling that the slope is $-\psi l/d$, and hence $-d\eta = \frac{d}{\psi l}\, d\xi$, the axial equilibrium of the portion of the bunch between the cuts reads

$$-\sum_{h=1}^{n_b} N_h + \frac{1}{\psi l}\int_{-l/2}^{l/2} N(\xi)\, d\xi - \int_{-l/2}^{l(1/2-\psi)} t_{i,j-1,k}(\xi)\, d\xi + \int_{l(1/2-\psi)}^{l/2} t_{i+1,j-1,k}(\xi)\, d\xi = 0. \tag{3.6}$$

Observe now that the latter two terms of (3.6) correspond to the resultant of the shear forces acting on the lower part of the CNT, i.e., T_{y^-} of Eq. (2.6), that is nil as per Eq. (2.7). This allows to evaluate the axial force on the bunch as

$$N_b = \sum_{h=1}^{n_b} N_h = \frac{1}{\psi l}\int_{-l/2}^{l/2} N(\xi)\, d\xi. \tag{3.7}$$

Eq. (3.7) may be regarded a generalization of Eq. (3.3), allowing to evaluate the axial force N_b acting on the bunch as the integral of the axial force $N(\xi)$ acting on the whole length of the constituent CNTs.

Remarkably, this expression can be used for arbitrary values of ψ. However, in this case, unless $1/\psi$ is an integer, it is obviously not possible to define a bunch composed of an integer number of CNTs. Consequently, N_b may be interpreted as the resulting axial force on a fiber portion, lying on the (x, y) plane, of height d/ψ and "thickness" d (in the z direction). Henceforth, its "area of competence" is again given by (3.4), and the total force on the whole fiber may be evaluated with an expression analogue to (3.5), i.e.,

$$N_f = \frac{A_f}{ld^2}\int_{-l/2}^{l/2} N(\xi)\, d\xi\,, \tag{3.8}$$

while the effective Young's modulus of the fiber (3.1) may be evaluated as

$$E_f = \frac{1}{\epsilon l d^2}\int_{-l/2}^{l/2} N(\xi)\, d\xi. \tag{3.9}$$

This confirms that, as expected, the effective Young's modulus is independent on size and shape of the fiber cross section, being dependent only on the geometrical and mechanical properties of the constituent CNTs, and on their lateral bond.

3.3. Results and comparisons

Once the axial strain and the axial load on the individual CNTs has been numerically evaluated as detailed in Section 2, the effective Young's modulus of the fiber can be calculated by means of Eq. (3.9). Here, the obtained results are compared with those obtained by using the simplified model of [41], assuming rigid CNTs, as well as with experimental data from literature.

3.3.1. Influence of mechanical and geometric parameters

To evaluate the influence of the diverse geometric and mechanical parameters, observe that, by recalling that $\int_{-l/2}^{l/2} N(\xi)\, d\xi = EA\int_{-l/2}^{l/2} u'(\xi)\, d\xi = EA\Delta l$, Eq. (3.9) may be rearranged as

$$E_f = \frac{\kappa\beta}{d^2}\,\phi(\beta, l, \psi). \tag{3.10}$$

where, again, $\beta = EA/\kappa$, and the non-dimensional function $\phi(\beta, l, \psi)$ is given by (2.9). It may be verified that the fiber axial modulus is intermediate between the following limits:

- when the CNTs are rigid ($EA \to \infty$), $\beta \to \infty$ and $\phi(\beta, l, \psi) \to 0$. In this case, it may be verified that

$$\beta\,\phi(\beta, l, \psi) \to 2\psi(1-\psi)l^2 \quad \Rightarrow \quad \lim_{\beta\to\infty} E_f = 2\kappa\psi(1-\psi)\frac{l^2}{d^2}, \tag{3.11}$$

  that coincides with the expression recorded in [41]. The details of the calculation are recorded in Appendix A.2.
- when the shear springs are rigid, i.e., $\kappa \to \infty$, $\beta \to 0$. In this case, as discussed in Section 2.4.2, $\phi(\beta, l, \psi) \to 1$ and

$$\lim_{\beta\to 0} E_f = \frac{EA}{d^2}. \tag{3.12}$$

  Notice that, since the quantity A/d^2 is the ratio between the CNTs cross sectional area and its "area of competence" in the cross section of the fiber, the effective fiber stiffness simply corresponds to the sum of the axial stiffness of the (fully coupled) individual CNTs.

In Fig. 15, the non-dimensional function $\phi(\beta, l, \psi)$ is plotted, as a function of β, for different values of ψ. The different graphs correspond to different CNT length. It is evident that $\phi(\beta, l, \psi) \to 1$ for low values of β, also dependently on the values of ψ and l. As expected, the ratio between the axial stiffness EA of the individual CNTs, and the stiffness κ of the distributed springs, plays a definite role on the fiber response. When the CNTs are bonded by means of cross-link, κ may be evaluated as a function of the cross-link density [45,47].

Remarkably, graphs in Fig. 15 may represent a practical tool to evaluate the effective stiffness of CNT fibers. Indeed, if the geometric

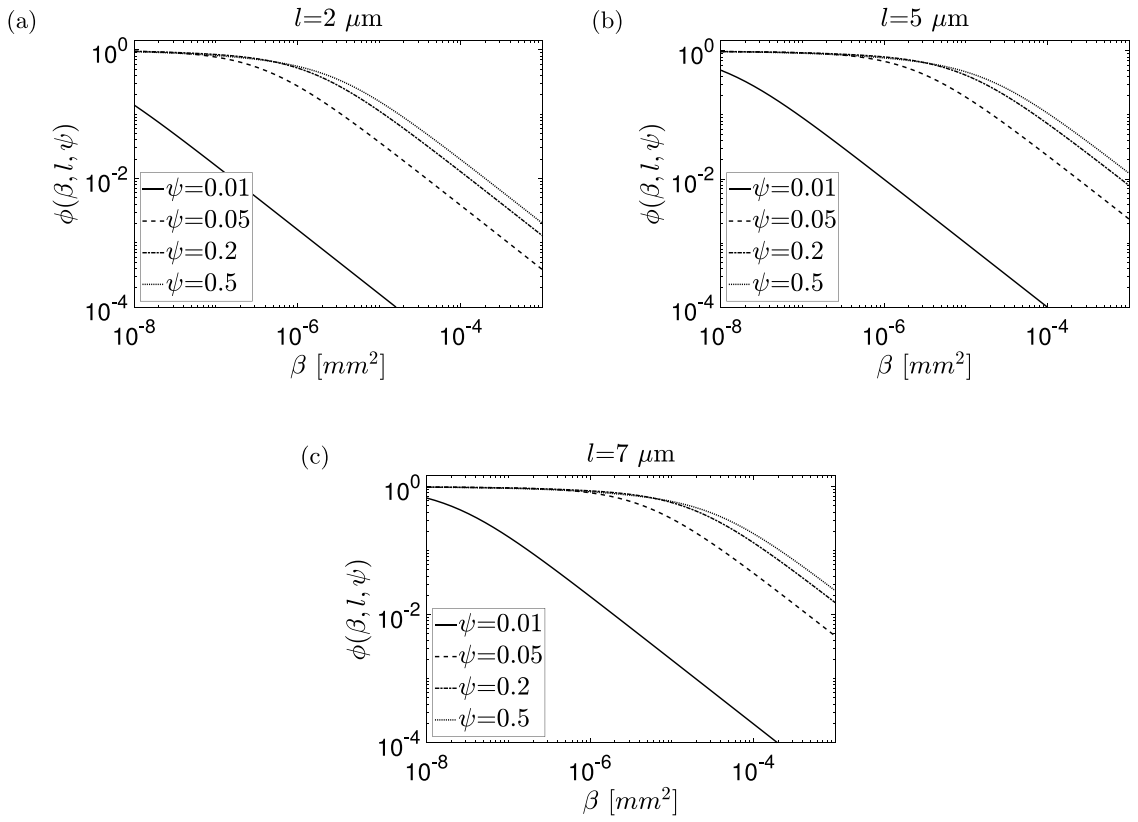

Fig. 15. Evaluation of $\phi(\beta, l, \psi)$, as a function of $\beta = EA/\kappa$, for different values of ψ, for CNT length of (a) 2 μm, (b) 5 μm and (c) 7 μm.

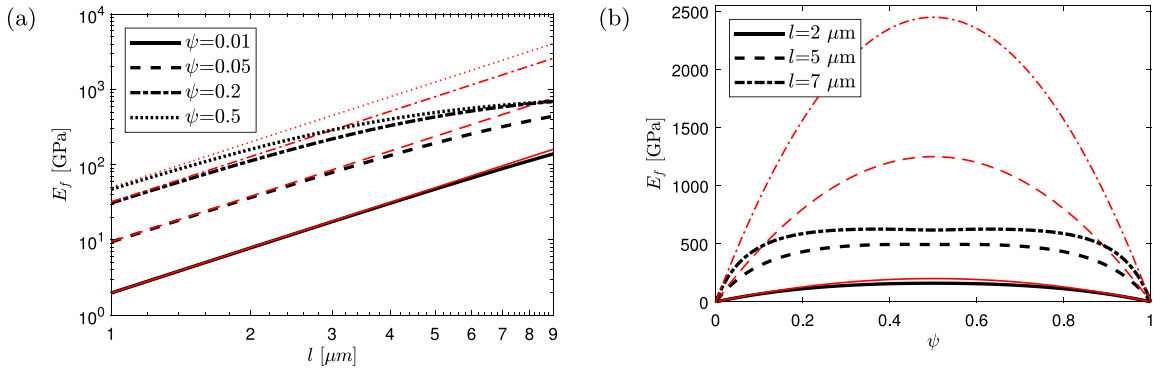

Fig. 16. Effective Young's modulus E_f of the CNT fiber (a) as a function of l, for different ψ, and (b) as a function of ψ, for different l: proposed model (thick black curves) and model by [41] (thin red curves).

(l, ψ) and mechanical (E, A, κ) parameters are known, these allow to evaluate the non-dimensional function $\phi(\beta, l, \psi)$ and, consequently, E_f through Eq. (3.10).

3.3.2. Comparison with the results obtained for the case of rigid CNTs

Here, the effective Young's modulus (3.9) is numerically evaluated for CNT fiber with the same geometric and mechanical parameters considered in Section 2.4.1, i.e., $d = 1$ nm, $s = 0.34$ nm, $E = 10^6$ MPa, $\kappa = 0.1$ MPa, and variable l and ψ. According to Eq. (3.9), the size of the fiber cross section does not affect its effective modulus.

Fig. 16(a) shows the effective Young's modulus E_f (plotted with thick black lines), on a logarithmic scale, as a function of the CNT length l. The different curves correspond to different values of the offset parameter ψ. To highlight the influence on the overall tensile response of the compliance of the CNTs, the results are compared with those obtained by assuming, as done in [41], the constituent CNTs to be rigid (3.11) (thin red curves).

As expected, when the offset parameter ψ increase, the coupling between the different CNTs increases, so providing an increase of macroscopic stiffness of the CNT fiber.

Notice that the model [41] provides an effective modulus directly proportional to the square of the length of the constituent CNTs, according to (3.11), so resulting in straight curves on the logarithmic plane. As may be noticed from Fig. 16(a), for low values of l, the proposed model provides results that in practice coincide with those of [41]. This is because, when the constituent CNTs are "short", their strain is very low (see also plot in Fig. 10(b)) and it does not affect the macroscopic stiffness. When l increases, the contribution of the deformability of the individual CNTs becomes more relevant, leading to a decrease of the overall axial stiffness of the fiber, with respect to that predicted by the model [41]. This results in a decrease of the slope of the curves in Fig. 16(a), that is more relevant for high values of the offset parameter ψ.

It can also be verified that, for very high values of the length l of the CNTs (dependently on the offset parameter, of the order of 10-20 μm, a value that cannot be obtained with the current technology), E_f settles to a constant value, independent on ψ. This means that when the CNTs are very long, they are "well coupled" because of their length, regardless of the offset, which becomes irrelevant under these conditions. This behavior is qualitatively similar to that observed in [41] for the *bending* response of CNT fibers.

Fig. 16(b) shows the effective Young's modulus E_f of the CNT fiber, plotted as a function of the offset parameter ψ, for various lengths l of the CNTs composing the fiber. Again, also the result obtained by assuming rigid CNTs are plotted for the sake of comparison. When CNTs are rigid, Eq. (3.11) provides a quadratic dependence of E_f on the offset parameter, with $E_f = 0$ for $\psi = 0, 1$ (configuration with stacked CNTs). The proposed model (Eq. (3.9)) provides a qualitatively different trend of E_f: the stiffness is still null for $\psi = 0, 1$, but the middle part of the graph is more "flattened". This behavior suggests that also values of ψ quite distant from 0.5 are sufficient to impart to the fiber an high coupling. This phenomenon is more marked for high values of l, confirming the conclusions drawn from Fig. 16(a).

It may be noticed that, since E_f is proportional to $\int_{-l/2}^{l/2} N(\xi)\, d\xi$, it has the same qualitative dependence on ψ and l of the function $\phi(\beta, l, \psi)$ plotted in Fig. 10(a). In particular, for higher values of l, E_f has a slight decrease for $\psi = 0.5$. This is because, as discussed in Section 2.4.2, for $\psi = 0.5$ the central region of the CNT is overstrained, so resulting in a decrease of the effective stiffness.

3.3.3. Comparison with experimental results

The obtained results are now compared with those recorded in the technical literature. Usually, experimental papers report measures of the effective axial stiffness of CNT fibers, sometimes indicating the (mean) values of d and l, but with no consideration of the offset parameter ψ. Indeed, real fibers are composed of CNTs with different lengths, randomly aggregated. The proposed model interprets this random phenomenon by the parameter ψ, which can be varied to obtain a range of values for the effective Young's modulus, within which the experimental results should fall.

In the sequel, reference is made to the accurate experimental results recorded in [71]. These refer to tensile tests, performed with a rheometer, on 3 cm long fibers, with circular cross section of diameter 10 μm, composed of single-walled CNTs with $d \simeq 1.5$ nm and different values of (mean) length l, i.e., 2.21 μm, 4.17 μm and 6.28 μm. Results presented in the sequel have been evaluated by considering a shear stiffness[9] of the lateral bonding $\kappa = 0.1$ Mpa, and a thickness of the graphite layer $s = 0.34$ nm. Fig. 17 shows the comparison between the effective modulus E_f (3.9) and the experimental results recorded in [71].

The proposed model seems to correctly capture not only the order of magnitude of the experimental results (the experimental data fall within the band of values provided by the proposed model), but also the decrease in the curve slope for increasing CNTs length. It may be noticed that, for 2.21 μm and 4.17 μm long CNTs, the offset parameter is near to 0.2, while it decreases with increasing length. As observed in [41], this theoretical prediction may be justified by the particular production process [31], in which long CNTs, having a limited mobility with respect to short CNTs, may tend to gather in bunches. It may be easily verified, by comparing Fig. 17 with Fig. 16(a), that the proposed model provides a better fit of the experimental data, with respect to the model assuming rigid CNTs [41], in particular for high values of l. This confirms that, when CNTs are "long", their axial strain becomes more relevant, and to neglect it leads to an underestimation of the macroscopic stiffness of the fiber.

[9] Again, since no precise data on the shear stiffness of the bonding are available, the value for κ recorded in [41] is here considered.

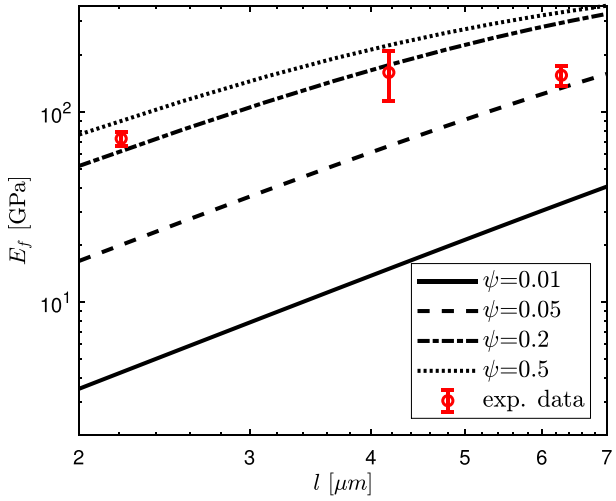

Fig. 17. Effective Young's modulus E_f of the CNT fiber as a function of l, for different ψ: comparison among the proposed model and experimental data from [71].

4. Conclusions

The paper presents an analytical–numerical micromechanical model for the evaluation of the tensile stiffness of Carbon NanoTube (CNT) fibers, accounting for the coupling occurring on their lateral surfaces, thanks to van der Waals forces and to cross-links. CNTs are modeled as bars with a given axial compliance, a factor neglected in most models previously proposed by the literature. The proposed model is based on the consideration that, due to the periodicity of the considered geometry, the same loading state is defined on each CNT composing the fiber, hence resulting in the same axial strain/stress field. It is demonstrated that these are governed by a delayed-advanced differential equation, here solved with finite difference technique. An analytical procedure has been presented to evaluate the resultant, on the whole fiber, of the axial forces on the individual CNTs, allowing to define the *macroscopic (effective) stiffness* of the fiber. It is demonstrated that this increases with the length of the CNTs and their axial offset, reaching its highest values when the latter is near to the half of the CNTs length. Graphs allowing to evaluate the effective stiffness of CNT fibers, as a function of geometric and mechanical parameters, are recorded.

The obtained results are in good agreement with the literature experimental data [71]. The accuracy of the model is found to be higher than that obtained by neglecting the axial compliance of the CNTs [41]. Thus, this represents an important step forward in the study of CNT fibers response, of particular importance in view of their use to produce cables for large-scale structural purposes. In particular, as technology is moving toward the production of longer CNTs, it is of particular importance to correctly account for the CNTs compliance. Further developments can consider more complex arrangements of CNTs, and the non-linear response of the connection between adjacent CNTs. With minor modifications, the proposed model could be suitable for the description of other structures composed of aligned nano-components, as for example boron nitride NTs [72].

Data availability

No data was used for the research described in the article.

Acknowledgments

This research did not receive any specific grant from funding agencies in the public, commercial, or not-for-profit sectors. Vincenzo Andrea Muratore gratefully acknowledges the partial funding by DexMat,

Inc. of his scholarship to attend the PhD program in Industrial Engineering at the University of Parma. The authors also acknowledge professor Gianni Royer-Carfagni for his precious comments and suggestions. All authors approved the version of the manuscript to be published.

Appendix

A.1. Analytical evaluation of the shear forces transmitted by the distributed springs

By considering the generic (i,j,k)th nanotube, whose centroid has axial coordinate $x_{G;i,j,k}$, the axial coordinates of the centroids of the adjacent CNTs on the (x,y) plane, shown in Fig. A.1(a), are

$$x_{G;i,j+1,k} = x_{G;i,j,k} + \psi l, \qquad x_{G;i-1,j+1,k} = x_{G;i,j,k} - (1-\psi) l,$$
$$x_{G;i,j-1,k} = x_{G;i,j,k} - \psi l, \qquad x_{G;i+1,j-1,k} = x_{G;i,j,k} + (1-\psi) l. \tag{A.1}$$

Consequently, by denoting by ξ the local axial coordinate defined on the (i,j,k)th CNT (see Fig. A.1(a)), the local coordinates defined on the four adjacent CNTs are

$$\xi_{i,j+1,k} = \xi - \psi l, \qquad \xi_{i-1,j+1,k} = \xi + (1-\psi) l,$$
$$\xi_{i,j-1,k} = \xi + \psi l, \qquad \xi_{i+1,j-1,k} = \xi - (1-\psi) l. \tag{A.2}$$

Since the CNTs distribution on the (x,y) and on the (x,z) planes is the same, due to the symmetry of the problem (see Fig. 2), relations analogue to (A.2) may be written by considering CNTs adjacent to the (i,j,k)th one, lying on the (x,z) plane.

As discussed in Section 2.2, the mesoscopic deformation of the fiber produces the two mechanisms schematized in Fig. A.1(b), i.e., the CNT elongation (highlighted by the darker regions in Fig. A.1(b)), due to the forces transmitted by the springs, and their axial displacement. The latter is proportional to the macroscopic stretch ϵ prescribed to the fiber, and consequently the position of the centroid of the (i,j,k)th CNT in the deformed configuration is $x_{G;i,j,k}(1+\epsilon)$, as shown in Fig. A.1(b).

To evaluate the relative slip between adjacent CNTs, consider first the arrangement on the (x,y) plane, as indicated in Fig. A.1(b). Consider the generic points P_0 and P_1, belonging to the (i,j,k)th and $(i,j+1,k)$th CNTs, respectively, and initially having the same axial position, as shown in Fig. A.1(a). By denoting by $u(\xi)$ the axial displacement at the local coordinate ξ, the position of P_0 after the deformation will be $x_{G;i,j,k}(1+\epsilon) + \xi + u(\xi)$. Since, as discussed in Section 2.2, the axial displacement field $u(\xi)$ is the same on each CNT, the axial position of P_1 after the deformation will be $(x_{G;i,j,k} + \psi l)(1+\epsilon) + (\xi - \psi l) + u(\xi - \psi l)$ (see Fig. A.1(b)). The reciprocal sliding between P_0 and P_1 may be evaluated simply as the difference between their final positions, and reads

$$\delta_{i,j+1,k}(\xi) = \psi l \epsilon + u(\xi - \psi l) - u(\xi), \tag{A.3}$$

while, analogously, the relative slip of the (i,j,k)th CNT with the other adjacent CNTs are

$$\delta_{i-1,j+1,k}(\xi) = -(1-\psi) l \epsilon + u(\xi + (1-\psi) l) - u(\xi),$$
$$\delta_{i,j-1,k}(\xi) = -\psi l \epsilon + u(\xi + \psi l) - u(\xi),$$
$$\delta_{i+1,j-1,k}(\xi) = (1-\psi) l \epsilon + u(\xi - (1-\psi) l) - u(\xi). \tag{A.4}$$

Consequently, the forces (per unit length) transmitted by the springs, of stiffness κ, connecting the CNT to the adjacent ones, on the (x,y) plane, may be written as

$$t_{i,j+1,k}(\xi) = \kappa\ \delta_{i,j+1,k}(\xi) = \kappa\,[\psi l \epsilon + u(\xi - \psi l) - u(\xi)]\,,$$
$$t_{i-1,j+1,k}(\xi) = \kappa\ \delta_{i-1,j+1,k}(\xi) = \kappa\,[-(1-\psi) l \epsilon + u(\xi + (1-\psi) l) - u(\xi)]\,,$$
$$t_{i,j-1,k}(\xi) = \kappa\ \delta_{i,j-1,k}(\xi) = \kappa\,[-\psi l \epsilon + u(\xi + \psi l) - u(\xi)]\,,$$
$$t_{i+1,j-1,k}(\xi) = \kappa\ \delta_{i+1,j-1,k}(\xi) = \kappa\,[(1-\psi) l \epsilon + u(\xi - (1-\psi) l) - u(\xi)]\,. \tag{A.5}$$

The forces transmitted by CNTs connected to the (i,j,k)th nanotube on the (x,z) plane are analogue to that on the (x,y) plane, and read

$$t_{i,j,k+1}(\xi) = \kappa\,[\psi l \epsilon + u(\xi - \psi l) - u(\xi)]\,,$$
$$t_{i-1,j,k+1}(\xi) = \kappa\,[-(1-\psi) l \epsilon + u(\xi + (1-\psi) l) - u(\xi)]\,,$$
$$t_{i,j,k-1}(\xi) = \kappa\,[-\psi l \epsilon + u(\xi + \psi l) - u(\xi)]\,,$$
$$t_{i+1,j,k-1}(\xi) = \kappa\,[(1-\psi) l \epsilon + u(\xi - (1-\psi) l) - u(\xi)]\,. \tag{A.6}$$

In the three regions schematically indicated in Fig. 3(a), the (i,j,k)th is connected with different adjacent CNTs, namely:

- region A: $(i-1,j+1,k)$, $(i,j-1,k)$, $(i-1,j,k+1)$, $(i,j,k-1)$ CNTs;
- region B: $(i,j+1,k)$, $(i,j-1,k)$, $(i,j,k+1)$, $(i,j,k-1)$ CNTs;
- region C: $(i,j+1,k)$, $(i+1,j-1,k)$, $(i,j,k+1)$, $(i+1,j,k-1)$ CNTs.

Hence, the total force transmitted by the shear springs on the lateral surface of the CNT may be defined, in the three regions, as

$$t_{tot}(\xi) = \begin{cases} t_{i-1,j+1,k}(\xi) + t_{i,j-1,k}(\xi) + t_{i-1,j,k+1}(\xi) + t_{i,j,k-1}(\xi) & \text{in region } A, \\ t_{i,j+1,k}(\xi) + t_{i,j-1,k}(\xi) + t_{i,j,k+1}(\xi) + t_{i,j,k-1}(\xi) & \text{in region } B, \\ t_{i,j+1,k}(\xi) + t_{i+1,j-1,k}(\xi) + t_{i,j,k+1}(\xi) + t_{i+1,j,k-1}(\xi) & \text{in region } C. \end{cases} \tag{A.7}$$

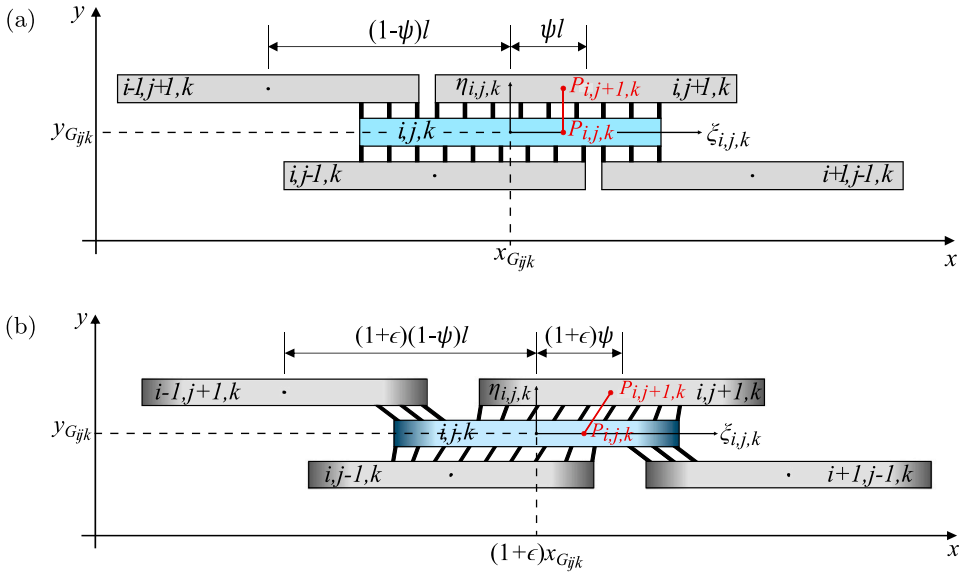

Fig. A.1. (a) Undeformed and (b) deformed configuration of adjacent CNTs, on the (x,y) plane, highlighting the axial displacement of the individual CNTs, and their axial strain.

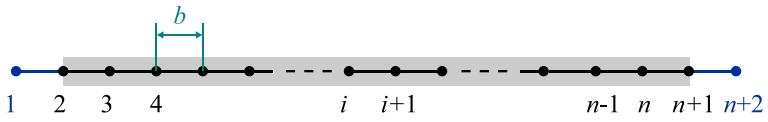

Fig. A.2. CNT discretization, with evidence of the "ghost nodes".

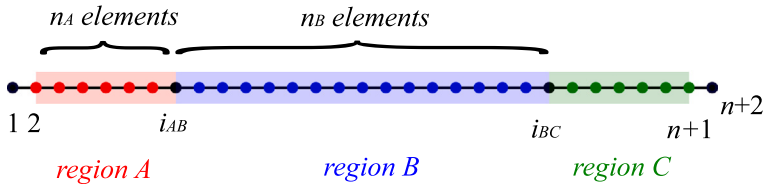

Fig. A.3. Discretization of CNT regions.

A.2. Analytical comparison with the case of rigid CNTs

If the CNTs composing the fiber are assumed to be rigid, as in [41], the governing equations turn out to be strongly simplified. Indeed, when the axial stiffness of the CNTs is assumed to be $EA \to \infty$, the axial displacement field $u(\xi)$ is identically nil, and the expressions for the shear forces transmitted by the distributed springs ((A.5) and (A.6)) may be simplified as follows:

$$\begin{aligned} t_{i,j+1,k} &= t_{i,j,k+1} = \kappa\psi l\epsilon, \\ t_{i-1,j+1,k} &= t_{i-1,j,k+1} = -\kappa(1-\psi) l\epsilon, \\ t_{i,j-1,k} &= t_{i,j,k-1} = -\kappa\psi l\epsilon, \\ t_{i+1,j-1,k} &= t_{i+1,j,k-1} = \kappa(1-\psi) l\epsilon, \end{aligned} \tag{A.8}$$

that coincide with expressions recorded in [41]. This allows to evaluate the total force transmitted on the lateral surface of the CNT, according to (A.7).

The axial force in each CNT may be evaluated by means of the equilibrium relation (2.3), with boundary conditions (2.5) (null axial force at the CNT's ends), and by requiring the continuity of $N(\xi)$ at the interfaces between adjacent regions. It may be verified that it takes the following expression:

$$\begin{cases} N(\xi) = \kappa\epsilon l(l+2\xi) & \text{in region } A, \\ N(\xi) = 2\kappa\epsilon\psi l^2 & \text{in region } B, \\ N(\xi) = \kappa\epsilon l(l-2\xi) & \text{in region } C. \end{cases} \tag{A.9}$$

It has been numerically verified that the obtained solution, in terms of $N(\xi)$, coincide with this closed form expression, when a very high value for the axial stiffness of the individual CNTs is set, i.e., for $EA \to \infty$.

If the constituent CNTs are assumed to be rigid, as in [41], their axial force $N(\xi)$ cannot be found from their constitutive law (2.2). This is why in [41] the axial force in the whole fiber is evaluated as the resultant of the shear interactions, by performing a "step-cut" of the fiber, not intersecting the CNTs. However, $N(\xi)$ may be recovered from the equilibrium of the individual CNTs, and it turns out to be in the form (A.9). The proposed approach hence allows to calculate N_f as the resultant of the axial forces on the individual CNTs by means of Eq. (3.8), providing the following expression:

$$N_f = 2\ A_f \kappa\epsilon\ \frac{l^2}{d^2}\psi(1-\psi). \tag{A.10}$$

The stiffness of the CNT fiber may be obtained by means of Eq. (3.1), providing an expression that coincide with (3.11) obtained in [41].

A.3. Implementation of the finite difference model

The determination of the axial displacement field in the CNTs composing the fiber is governed by the "delayed advanced differential equation" (2.4), i.e., a differential equation in which the unknown function and its derivatives at a given point in the domain depend on the values taken by the function itself at "previous" and "subsequent" points, in terms of the axial coordinate. Because of the high complexity, these kinds of equations are usually solved by numerical techniques [60].

Here, the solution is found by implementing (2.4) with a finite difference technique. The considered CNT is discretized by dividing it into $n_e = n-1$ elements, where n is the number of nodes[10], of the same length b. To treat Neumann boundary conditions (2.5) in an accurate way, it is necessary to add two "ghost nodes" (see, among the others, [73,74]) outside of the domain and next to the boundaries, as shown in Fig. A.2. This obviously results in a total number of $n+2$ nodes.

The displacement field in the CNT is described by a vector $\mathbf{u}$, whose components are denoted in the sequel as u_i, $i = 1 \dots n{+}2$. Notice that this choice ensure the continuity of the axial displacement at the interfaces between the different regions. In the interior of the computational domain the second derivative is defined by using the "second central difference" scheme, i.e.,

$$u''(\xi) \ \Rightarrow \ \frac{u_{(i+1)} - 2u_i + u_{(i-1)}}{b^2}, \tag{A.11}$$

while boundary conditions (2.5) are prescribed by using the "backward difference" and "forward difference" schemes at the two ends of the domain, respectively, i.e.,

$$\frac{u_2 - u_1}{b} = 0, \quad \frac{u_{(n+2)} - u_{(n+1)}}{b} = 0. \tag{A.12}$$

The numbers of elements in region A, n_A, and B, n_B, are respectively given by

$$n_A = \psi\ n_e \quad n_B = (1-2\psi)\ n_e. \tag{A.13}$$

Hence, the boundary nodes between regions A and B, and between B and C, are located at $i_{AB} = n_A + 2$ and $i_{BC} = n_A + n_B + 2$, as schematized in Fig. A.3. Obviously, for $\psi = 0.5$ the end of region A coincides with the beginning of region C, while the length of region B is nil. Henceforth, in the numerical code $i_{AB} = i_{BC}$.

To avoid ambiguities, the continuity of the axial force $N(\xi)$, i.e., the equality between the backward and the forward first derivative of $u(\xi)$, is prescribed at the interface nodes i_{AB} and i_{BC}, in the form

$$\frac{u_i - u_{(i-1)}}{b} = \frac{u_{(i+1)} - u_i}{b} \qquad i = i_{AB},\ i_{BC}, \tag{A.14}$$

[10] To have a symmetrical configuration with respect to the central node, n is chosen to be an odd number.

while the field Eqs. (2.4) are prescribed on the three regions in the form

$$\begin{cases} EA\frac{u_{(i+1)}-2u_i+u_{(i-1)}}{b^2} = 2k(\varepsilon l - u_{(i+n_A)} - u_{(i+n_A+n_B)} + 2\ u_i) & \forall i \in [2, i_{AB}-1] \\ EA\frac{u_{(i+1)}-2u_i+u_{(i-1)}}{b^2} = 2k(u_{(i+n_A)} - u_{(i-n_A)} + 2\ u_i) & \forall i \in [i_{AB}+1, i_{BC}-1] \\ EA\frac{u_{(i+1)}-2u_i+u_{(i-1)}}{b^2} = -2k(\varepsilon l - u_{(i-n_A-n_B)} - u_{(i-n_A)} + 2\ u_i), & \forall \in [i_{BC}+1, n+1]. \end{cases} \tag{A.15}$$

To avoid rigid body displacements, the displacement of the central node has been set equal to zero. Eq. (A.15) may be rearranged in a matrix form as $\mathbf{Ku} = \mathbf{b}$, where $\mathbf{K}$ is the matrix of coefficients, $\mathbf{u}$ is the vector of unknown nodal displacements, and $\mathbf{b}$ is the vector of known terms. It may be verified that $\mathbf{K}$ is a banded matrix.

References

[1] Iijima S. Helical microtubules of graphitic carbon. Nature 1991;354(6348):56–8.
[2] Iijima S, Ichihashi T. Single-shell carbon nanotubes of 1-nm diameter. Nature 1993;363(6430):603–5.
[3] Su DS. 20 Years of carbon nanotubes. 2011.
[4] Popov VN. Carbon nanotubes: properties and application. Mater Sci Eng R 2004;43(3):61–102.
[5] Arepalli S, Nikolaev P, Gorelik O, Hadjiev VG, Holmes W, Files B, et al. Protocol for the characterization of single-wall carbon nanotube material quality. Carbon 2004;42(8–9):1783–91.
[6] Ibrahim KS. Carbon nanotubes-properties and applications: a review. Carbon Lett 2013;14(3):131–44.
[7] Nakayama Y, Akita S. Nanoengineering of carbon nanotubes for nanotools. New J Phys 2003;5(1):128.
[8] Davis VA, Parra-Vasquez ANG, Green MJ, Rai PK, Behabtu N, Prieto V, et al. True solutions of single-walled carbon nanotubes for assembly into macroscopic materials. Nature Nanotechnol 2009;4(12):830–4.
[9] McEuen PL, Fuhrer MS, Park H. Single-walled carbon nanotube electronics. IEEE Trans Nanotechnol 2002;1(1):78–85.
[10] Wang C, Takei K, Takahashi T, Javey A. Carbon nanotube electronics–moving forward. Chem Soc Rev 2013;42(7):2592–609.
[11] Eatemadi A, Daraee H, Karimkhanloo H, Kouhi M, Zarghami N, Akbarzadeh A, et al. Carbon nanotubes: properties, synthesis, purification, and medical applications. Nanoscale Res Lett 2014;9(1):1–13.
[12] Raphey V, Henna T, Nivitha K, Mufeedha P, Sabu C, Pramod K. Advanced biomedical applications of carbon nanotube. Mater Sci Eng C 2019;100:616–30.
[13] Treacy MJ, Ebbesen TW, Gibson JM. Exceptionally high Young's modulus observed for individual carbon nanotubes. Nature 1996;381(6584):678–80.
[14] Krishnan A, Dujardin E, Ebbesen T, Yianilos P, Treacy M. Young's modulus of single-walled nanotubes. Phys Rev B 1998;58(20):14013.
[15] Wu J, He J, Odegard GM, Nagao S, Zheng Q, Zhang Z. Giant stretchability and reversibility of tightly wound helical carbon nanotubes. J Am Chem Soc 2013;135(37):13775–85.
[16] Wu J, Shi Q, Zhang Z, Wu H-H, Wang C, Ning F, et al. Nature-inspired entwined coiled carbon mechanical metamaterials: molecular dynamics simulations. Nanoscale 2018;10(33):15641–53.
[17] Moniruzzaman M, Winey KI. Polymer nanocomposites containing carbon nanotubes. Macromolecules 2006;39(16):5194–205.
[18] Mittal V. Polymer nanotubes nanocomposites: synthesis, properties and applications. John Wiley & Sons; 2014.
[19] Chen J, Liu B, Gao X, Xu D. A review of the interfacial characteristics of polymer nanocomposites containing carbon nanotubes. RSC Adv. 2018;8(49):28048–85.
[20] Goh P, Ismail A, Ng B. Directional alignment of carbon nanotubes in polymer matrices: Contemporary approaches and future advances. Composites A 2014;56:103–26.
[21] Liu M, Younes H, Hong H, Peterson G. Polymer nanocomposites with improved mechanical and thermal properties by magnetically aligned carbon nanotubes. Polymer 2019;166:81–7.
[22] Pipes RB, Hubert P, Salvetat J-P, Zalamea L. Flexural deflection as a measure of van der Waals interaction forces in the CNT array. Compos Sci Technol 2006;66(9):1125–31.
[23] Acquah S, Ventura D, Kroto H. Strategies to successfully cross-link carbon nanotubes. In: Electronic properties of carbon nanotubes. IntechOpen; 2011.
[24] Park O-K, Choi H, Jeong H, Jung Y, Yu J, Lee JK, et al. High-modulus and strength carbon nanotube fibers using molecular cross-linking. Carbon 2017;118:413–21.
[25] Vigolo B, Penicaud A, Coulon C, Sauder C, Pailler R, Journet C, et al. Macroscopic fibers and ribbons of oriented carbon nanotubes. Science 2000;290(5495):1331–4.
[26] Ericson H, Fan H, Peng VA, Davis W, Zhou J, Sulpizio Y, et al. Macroscopic, neat, single-walled carbon nanotube fibers. Science 2004;305(5689):1447–50.
[27] Jiang K, Li Q, Fan S. Spinning continuous carbon nanotube yarns. Nature 2002;419(6909):801.
[28] Zhu H, Xu C, Wu D, Wei B, Vajtai R, Ajayan P. Direct synthesis of long single-walled carbon nanotube strands. Science 2002;296(5569):884–6.
[29] Behabtu N, Green MJ, Pasquali M. Carbon nanotube-based neat fibers. Nano today 2008;3(5–6):24–34.
[30] Headrick RJ, Tsentalovich DE, Berdegué J, Bengio EA, Liberman L, Kleinerman O, et al. Structure–property relations in carbon nanotube fibers by downscaling solution processing. Adv Mater 2018;30(9):1704482.
[31] Behabtu N, Young CC, Tsentalovich DE, Kleinerman O, Wang X, Ma AW, et al. Strong, light, multifunctional fibers of carbon nanotubes with ultrahigh conductivity. Science 2013;339(6116):182–6.
[32] Taylor LW, Dewey OS, Headrick RJ, Komatsu N, Peraca NM, Wehmeyer G, et al. Improved properties, increased production, and the path to broad adoption of carbon nanotube fibers. Carbon 2021;171:689–94.
[33] Wu J, Nagao S, He J, Zhang Z. Nanohinge-induced plasticity of helical carbon nanotubes. Small 2013;9(21):3561–6.
[34] Wu J, Zhao H, Liu J, Zhang Z, Ning F, Liu Y. Nanotube-chirality-controlled tensile characteristics in coiled carbon metastructures. Carbon 2018;133:335–49.
[35] Li K, Eres G, Howe J, Chuang Y-J, Li X, Gu Z, et al. Self-assembly of graphene on carbon nanotube surfaces. Sci Rep 2013;3(1):1–4.
[36] Gao W, Komatsu N, Taylor LW, Naik GV, Yanagi K, Pasquali M, et al. Macroscopically aligned carbon nanotubes for flexible and high-temperature electronics, optoelectronics, and thermoelectrics. J Phys D: Appl Phys 2019;53(6):063001.
[37] McCauley MD, Vitale F, Yan JS, Young CC, Greet B, Orecchioni M, et al. In vivo restoration of myocardial conduction with carbon nanotube fibers. Circ: Arrhythm Electrophysiol 2019;12(8):e007256.
[38] Yan JS, Orecchioni M, Vitale F, Coco JA, Duret G, Antonucci S, et al. Biocompatibility studies of macroscopic fibers made from carbon nanotubes: Implications for carbon nanotube macrostructures in biomedical applications. Carbon 2021;173:462–76.
[39] DesRoches R, Migliaccio G, Royer-Carfagni G. Structures that can be made with carbon nanotube fibers but not with other materials. J Eng Mech 2022;148(12):04022077.
[40] Migliaccio G, DesRoches R, Royer-Carfagni G. Theoretical mechanical properties of strands and cables made of wound carbon nanotube fibers. Int J Mech Sci 2022;107706.
[41] Galuppi L, Pasquali M, Royer-Carfagni G. The effective tensile and bending stiffness of nanotube fibers. Int J Mech Sci 2019;163:105089.
[42] Liew K, Wong C, Tan M. Tensile and compressive properties of carbon nanotube bundles. Acta Mater 2006;54(1):225–31.
[43] Gspann TS, Montinaro N, Pantano A, Elliott JA, Windle AH. Mechanical properties of carbon nanotube fibres: St Venant's principle at the limit and the role of imperfections. Carbon 2015;93:1021–33.
[44] Liu X, Lu W, Ayala OM, Wang L-P, Karlsson AM, Yang Q, et al. Microstructural evolution of carbon nanotube fibers: deformation and strength mechanism. Nanoscale 2013;5(5):2002–8.
[45] Zhang Z, Liu B, Zhang Y-W, Hwang K-C, Gao H. Ultra-strong collagen-mimic carbon nanotube bundles. Carbon 2014;77:1040–53.
[46] Wei X, Naraghi M, Espinosa HD. Optimal length scales emerging from shear load transfer in natural materials: application to carbon-based nanocomposite design. ACS nano 2012;6(3):2333–44.
[47] Sun X, Zhang Z, Xu Y, Zhang Y. An elastic model for bioinspired design of carbon nanotube bundles. Acta Mech Sin 2015;31(2):205–15.
[48] Mählich D, Eberhardt O, Wallmersperger T. Numerical simulation of the mechanical behavior of a carbon nanotube bundle. Acta Mech. 2021;232(2):483–94.
[49] Eringen AC, Edelen DGB. On nonlocal elasticity. Int J Eng Sci 1972;10(3):233–48.
[50] Silling SA, Zimmermann M, Abeyaratne R. Deformation of a peridynamic bar. J Elasticity 2003;73(1):173–90.
[51] Emmrich E, Lehoucq RB, Puhst D. Peridynamics: a nonlocal continuum theory. In: Meshfree methods for partial differential equations VI. Springer; 2013, p. 45–65.
[52] Ostanin I, Ballarini R, Dumitrică T. Distinct element method modeling of carbon nanotube bundles with intertube sliding and dissipation. J Appl Mech 2014;81(6).
[53] Wei X, Ford M, Soler-Crespo RA, Espinosa HD. A new Monte Carlo model for predicting the mechanical properties of fiber yarns. J Mech Phys Solids 2015;84:325–35.
[54] Bathe M, Heussinger C, Claessens MM, Bausch AR, Frey E. Cytoskeletal bundle mechanics. Biophys J 2008;94(8):2955–64.
[55] Lin YW, Jiang WG, Chen LA, Liu WG, Zou H. A non-linear spring model for predicting modal behavior of oscillators built from double walled carbon nanotubes. J Nano Res 2019;60:21–32, Trans Tech Publ.
[56] Li C, Chou T-W. A structural mechanics approach for the analysis of carbon nanotubes. Int J Solids Struct 2003;40(10):2487–99.
[57] Li C, Chou T-W. Elastic moduli of multi-walled carbon nanotubes and the effect of van der Waals forces. Compos Sci Technol 2003;63(11):1517–24.
[58] Lu JP. Elastic properties of carbon nanotubes and nanoropes. Phys Rev Lett 1997;79(7):1297.

[59] Huang Y, Wu J, Hwang K-C. Thickness of graphene and single-wall carbon nanotubes. Phys Rev B 2006;74(24):245413.
[60] Iakovleva V, Vanegas CJ. On the solution of differential equations with delayed and advanced arguments. Electron J Differ Equ (EJDE)[Electronic Only] 2005;2005:57–63.
[61] Kyrychko Y, Hogan S. On the use of delay equations in engineering applications. J Vib Control 2010;16(7-8):943–60.
[62] Eringen AC. On differential equations of nonlocal elasticity and solutions of screw dislocation and surface waves. J Appl Phys 1983;54(9):4703–10.
[63] Aguiar AR, Patriota TVB, Royer-Carfagni G, Seitenfuss AB. Boundary layer effects in a finite linearly elastic peridynamic bar. Lat Am J Solids Struct 2018;15.
[64] Aguiar AR, Royer-Carfagni G, Seitenfuss AB. Wiggly strain localizations in peridynamic bars with non-convex potential. Int J Solids Struct 2018;138:1–12.
[65] Kosov A, Semenov E. On analytic periodic solutions to nonlinear differential equations with delay (advance). Russian Math 2018;62(10):30–6.
[66] Patidar KC, Sharma KK. Uniformly convergent non-standard finite difference methods for singularly perturbed differential-difference equations with delay and advance. Int J Numer Methods Eng 2006;66(2):272–96.
[67] Chiu K-S, Pinto M. Oscillatory and periodic solutions in alternately advanced and delayed differential equations. Carpathian J Math 2013;149–58.
[68] Li C, Liu Y, Yao X, Ito M, Noguchi T, Zheng Q. Interfacial shear strengths between carbon nanotubes. Nanotechnology 2010;21(11):115704.
[69] Kordkheili SH, Moshrefzadeh-Sani H. Mechanical properties of double-layered graphene sheets. Comput Mater Sci 2013;69:335–43.
[70] Lin M, Sun X, Xie W, Zhang Z. Load-transfer and failure behaviors of crosslinked interfaces in collagen-mimic carbon nanotube bundles. Int J Mech Sci 2018;135:376–82.
[71] Adnan M, Pinnick RA, Tang Z, Taylor LW, Pamulapati SS, Royer-Carfagni G, et al. Bending behavior of CNT fibers and their scaling laws. Soft Matter 2018;14(41):8284–92.
[72] Matatyaho Ya'akobi A, Ginestra CJ, Scammell LR, Smith MW, Pasquali M, Talmon Y. Electron microscopy study of BNNTs synthesized by high temperature–pressure method and purified by high-temperature steam. J Mater Res 2022;1–14.
[73] Coco A, Currenti G, Del Negro C, Russo G. A second order finite-difference ghost-point method for elasticity problems on unbounded domains with applications to volcanology. Commun Comput Phys 2014;16(4):983–1009.
[74] Renaudeau J, Irakarama M, Laurent G, Maerten F, Caumon G. Implicit modelling of geological structures: A cartesian grid method handling discontinuities with ghost points. WIT Trans Eng Sci 2019;122:189–99.